Article

A New XYZ Compliant Parallel Mechanism for Micro-/Nano-Manipulation: Design and Analysis

Haiyang Li, Guangbo Hao * and Richard C. Kavanagh

School of Engineering-Electrical and Electronic Engineering, University College Cork, Cork, Ireland; haiyang.li@umail.ucc.ie (H.L.); r.kavanagh@ucc.ie (R.C.K.)

* Corresponding: g.hao@ucc.ie; Tel.: +353-021-490-3793

Abstract: Based on the constraint and position identification (CPI) approach for synthesizing XYZ compliant parallel mechanisms (CPMs) and configuration modifications, this paper proposes a new fully-symmetrical XYZ CPM with desired motion characteristics such as reduced cross-axis coupling, minimized lost motion, and relatively small parasitic motion. The good motion characteristics arise from not only its symmetric configuration, but also the rigid linkages between non-adjacent rigid stages. Comprehensive kinematic analysis is carried out based on a series of finite element simulations over a motion range per axis less than $\pm 5\%$ of the beam length, which reveals that the maximum cross-axis coupling rate is less than 0.86%, the maximum lost motion rate is less than 1.20%, the parasitic rotations of the motion stage (MS) are in the order of 10^{-5} rad, and the parasitic translations of the three actuated stages (ASs) are in the order of 10^{-4} of the beam length (less than 0.3% of the motion range), where the beam slenderness ratio is larger than 20. Furthermore, the nonlinear analytical models of the primary translations of the XYZ CPM, including the primary translations of the MS and the ASs, are derived and validated to provide a quick design synthesis. Moreover, two practical design schemes of the proposed XYZ CPM are discussed with consideration of the manufacturability. The practical designs enable the XYZ CPM to be employed in many applications such as micro-/nano-positioning, micro-/nano-manufacturing and micro-/nano-assembly. Finally, a spatial high-precision translational system is presented based on the practical design schemes, taking the actuator and sensor integration into account.

Keywords: compliant parallel mechanism; micro-/nano-manipulation; conceptual design; kinematic analysis; analytical modeling; practical design

1. Introduction

Compliant mechanisms have no traditional sliding or rolling hinges, thereby lending advantages over rigid-body counterparts, such as no backlash, no requirement for lubrication, simplified manufacture, and low part count [1–8]. Currently, XYZ compliant parallel mechanisms (XYZ CPMs) are gaining more and more attention and are being widely employed in a variety of applications such as atomic force microscopy (AFM), micro-/nano-manipulation, high precision alignment, and microelectromechanical systems (MEMS) processes [6,9–16].

In most of the above applications, an XYZ CPM acts as a type of macro-scale mechatronic motion system, and its output motion stage (MS) should be capable of translating along the X-, Y- and Z-axes, with ultra-high precision [17]. However, compliant joints in an XYZ CPM are not ideal compared with their rigid-body counterparts. The stiffness of a compliant joint is neither zero in the degree of freedom (DOF) directions nor infinitely large in the degree of constraint (DOC) directions. Hence, an XYZ CPM often suffers from undesired parasitic motions and coupling motions [9,10]. For the MS of an XYZ

CPM as an example, the parasitic motions are the three rotations of the MS about the X-, Y- and Z-axes, which should be much smaller than its three primary translations.

An XYZ CPM is always actuated by three translational actuators, such as voice coils and piezoelectric stacks, exerted on the three actuated stages (ASs: AS-X, AS-Y and AS-Z along the three axes) [5,18]. As is well known, translational actuators cannot tolerate off-axis loads or displacements. Therefore, an AS is permitted to translate only along the actuation direction [9,18], the motions along and about the other directions are the parasitic motions of the AS. In order to protect the three translational actuators and achieve precise control in an XYZ CPM system, the parasitic rotations and the parasitic translations of the three ASs should be minimized.

The three desired translations of the MS and the one permitted translation of each AS in an XYZ CPM system are the primary translations of the XYZ CPM. Based on [9,11], the primary translations of an XYZ CPM should have the following desired characteristics: (a) reduced cross-axis coupling: the primary translation of an MS along one axis should be independent from the primary actuation along the other two axes; and (b) minimized lost motion: in the X-, Y- or Z-axis direction, the motion reduction between the primary translations of the AS and the MS should be minimized. All XYZ CPMs desire the above two primary translation characteristics, especially when closed-loop control systems are not available. The cross-axis coupling of an XYZ CPM can be measured by three cross-axis coupling rates regarding the three primary translations of the MS. When only one axis actuation is applied on an XYZ CPM, the primary translation of the MS along this axis is defined as the nominal primary translation of the MS along the axis. The primary translation of the MS will deviate from the nominal primary translation, if the other one or two actuations are applied. The ratio of the deviation to the nominal primary translation is termed the cross-axis coupling rate along this axis. The lost motions of an XYZ CPM, along the X-, Y- or Z-axes, can be represented as three lost motion rates. The lost motion rate along one axis is defined as the ratio of the motion reduction to the AS's primary translation along the axis.

As a result, the following attributes, Cross-Axis Coupling Rates, Lost Motion Rates, Parasitic Rotations and Parasitic Translations, can be used to measure the motion performance of an XYZ CPM. This paper defines the motions of an XYZ CPM as follows: MS's motions along and about the X-, Y- and Z-axes of the global coordinate system are ξ_{ms-tx}, ξ_{ms-ty}, ξ_{ms-tz}, ξ_{ms-rx}, ξ_{ms-ry} and ξ_{ms-rz}; AS-X's motions along and about the X-, Y- and Z-axes of the AS-X's local coordinate system are ξ_{asx-tx}, ξ_{asx-ty}, ξ_{asx-tz}, ξ_{asx-rx}, ξ_{asx-ry} and ξ_{asx-rz}; AS-Y's motions along and about the X-, Y- and Z-axes of the AS-Y's local coordinate system are ξ_{asy-tx}, ξ_{asy-ty}, ξ_{asy-tz}, ξ_{asy-rx}, ξ_{asy-ry} and ξ_{asy-rz}; AS-Z's motions along and about the X-, Y- and Z-axes of the AS-Z's local coordinate system are ξ_{asz-tx}, ξ_{asz-ty}, ξ_{asz-tz}, ξ_{asz-rx}, ξ_{asz-ry} and ξ_{asz-rz}. Note that the *X*-axes of the AS-X's, AS-Y's and AS-Z's local coordinate systems parallel to the X-, Y- and Z-axes of the global coordinate system, respectively. Therefore, the above four attributes of an XYZ CPM can be represented or calculated, as shown in Table 1. For a desired XYZ CPM, the above four attributes should be minimized. In addition, compact configuration and easy fabrication are also preferable [6].

Table 1. Representation or calculation of the four motion characteristics of an XYZ CPM.

Motion Characteristics	X-Axis	Y-Axis	Z-Axis
Cross-Axis Coupling Rates	$\lvert(\xi_{ms-tx} - \xi_{ms-tx}{}^{\circ})/\xi_{ms-tx}{}^{\circ}\rvert$	$\lvert(\xi_{ms-ty} - \xi_{ms-ty}{}^{\circ})/\xi_{ms-ty}{}^{\circ}\rvert$	$\lvert(\xi_{ms-tz} - \xi_{ms-tz}{}^{\circ})/\xi_{ms-tz}{}^{\circ}\rvert$
Lost Motion Rates	$(\xi_{asx-tx} - \xi_{ms-tx})/\xi_{asx-tx}$	$(\xi_{asy-tx} - \xi_{ms-ty})/\xi_{asy-tx}$	$(\xi_{asz-tx} - \xi_{ms-tx})/\xi_{asz-tx}$
Parasitic Rotations	ξ_{ms-rx}, ξ_{ms-ry}, ξ_{ms-rz}, ξ_{asx-rx}, ξ_{asx-ry}, ξ_{asx-rz}, ξ_{asy-rx}, ξ_{asy-ry}, ξ_{asy-rz}, ξ_{asz-rx}, ξ_{asz-ry}, ξ_{asz-rz}		
Parasitic Translations	ξ_{asx-ty}, ξ_{asx-tz}, ξ_{asy-ty}, ξ_{asy-tz}, ξ_{asz-ty}, ξ_{asz-tz}		

Notes: $\xi_{ms-tx}{}^{\circ}$, $\xi_{ms-ty}{}^{\circ}$ and $\xi_{ms-tz}{}^{\circ}$ represent, respectively, the ξ_{ms-tx} when $\xi_{ms-ty} = 0$ and $\xi_{ms-tz} = 0$, the ξ_{ms-ty} when $\xi_{ms-tx} = 0$ and $\xi_{ms-tz} = 0$, and the ξ_{ms-tz} when $\xi_{ms-tx} = 0$ and $\xi_{ms-ty} = 0$. "$\lvert\ \rvert$" denotes the absolute value of a number or a formula between the two vertical bars. For example, $\lvert(\xi_{ms-tx} - \xi_{ms-tx}{}^{\circ})/\xi_{ms-tx}\rvert$ indicates the absolute value of $(\xi_{ms-tx} - \xi_{ms-tx}{}^{\circ})/\xi_{ms-tx}$.

In recent years, many XYZ CPMs [6,9–12,18–20] have been designed using the pseudo-rigid-body-based model substitution approach [21], the constraint-based approach [22,23], the screw-theory-based approach [24], the freedom and constraint topology approach [25,26], and the CPI approach [18].

These existing XYZ CPMs have one or some of the four desired performance characteristics mentioned above. For example, the XYZ CPMs demonstrated in [6,9–12,18,20] have small cross-axis coupling attributes, and the XYZ CPM reported in [11] also has relative small parasitic rotations. However, none of the reported XYZ CPMs have all the four desired motion characteristics, because the design of such an XYZ CPM is still challenging.

This paper proposes a new XYZ CPM whose cross-axis coupling rates, lost motion rates, parasitic rotations and parasitic translations are minimized. The proposed XYZ CPM is synthesized using the CPI approach [18] with certain configuration modification, such as adding rigid linkages between some non-adjacent rigid stages [27,28]. The good motion characteristics of the designed XYZ CPM are validated by the finite element analysis (FEA) results. Moreover, the primary translations of the XYZ CPM are also nonlinearly modeled in an analytical form, which can offer quick quantitative and parametric insights into the actuation stiffness and the force-displacement relationship.

The remainder of this paper is organized as follows. Section 2 reviews the CPI approach of synthesizing XYZ CPMs. An XYZ CPM, in Section 3, is proposed based on the CPI approach. The kinematic analysis is carried out based on a series of FEA simulations in Section 4. The nonlinear analytical models of the primary translations are obtained and validated in Section 5. Furthermore, Section 6 shows two practical designs of the proposed XYZ CPM, and Section 7 introduces a spatial high-precision translational system designed based on practical designs. Finally, conclusions are drawn in Section 8.

2. CPI Approach Revisit

The CPI approach proposed in [18] can be employed to synthesize a variety of decoupled XYZ CPMs. The CPI approach decomposes an XYZ CPM into an MS, passive modules (PMs), active modules (AMs), ASs, and base stages (BSs). For a decoupled three-legged XYZ CPM in the CPI approach, the MS, the three PMs (PM-X, PM-Y and PM-Z), the three AMs (AM-X, AM-Y and AM-Z), the three ASs (AS-X, AS-Y and AS-Z), the three BSs (BS-X, BS-Y and BS-Z), and the coordinate systems are defined as demonstrated in Figure 1. The rigid stages, the MS, ASs and BSs, are all assumed to be perfectly rigid, and the compliant modules, AMs and PMs, can be designed on the basis of the constraints selected from the constraint space proposed in the CPI approach. Then, a decoupled three-legged XYZ CPM can be synthesized via assembling all the rigid stages and compliant modules together, based on their position spaces derived via the CPI approach. The constraint space and position space contain many permitted constraints and positions for each compliant module, so that a great number of decoupled three-legged XYZ CPMs can be synthesized using the CPI approach. Additionally, the designed three-legged XYZ CPMs can be further improved, for example by adding redundant legs, so that the resulting XYZ CPMs have good motion characteristics, compact configuration, easy manufacturability, and so on.
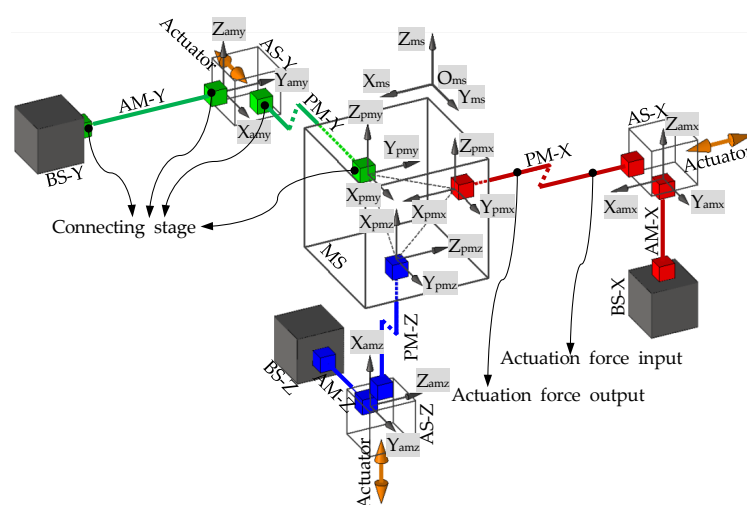

Figure 1. Schematic diagram of a decoupled three-legged XYZ CPM system and the coordinate systems.

3. Design of an XYZ CPM

In this section, the design of an XYZ CPM with the four aforementioned motion characteristics is considered. In order to do so, the CPI approach is followed, with consideration of compact configuration and easy manufacturability. The design procedure is demonstrated in the following steps:

1.　Select constraints for the PMs and AMs from the constraint space proposed in [18]. Note that the constraints are all described based on the global and local coordinate systems defined in Figure 1. For this case, the selected constraints of the PMs and AMs are illustrated in Table 2. According to the constraints selected, the three PMs or the three AMs in the three legs can be designed with the same structure, because the selected constraints of the PMs or the AMs have the same pattern in their own local coordinate systems.

Table 2. Constraints of the passive modules (PMs) and active modules (AMs) in the PM and AM local coordinate systems.

Module	Constraints of the PMs and AMs in the PM and AM Local Coordinate Systems		
	X-Leg	**Y-Leg**	**Z-Leg**
PMs	$T_{pmx-tx}R_{pmx-ry}R_{pmx-rz}$	$T_{pmy-tx}R_{pmy-ry}R_{pmy-rz}$	$T_{pmz-tx}R_{pmz-ry}R_{pmz-rz}$
AMs	$T_{amx-ty}T_{amx-tz}R_{amx-rx}R_{amx-ry}R_{ax-rz}$	$T_{amy-ty}T_{amy-tz}R_{amy-rx}R_{amy-ry}R_{amy-rz}$	$T_{amz-ty}T_{amz-tz}R_{amz-rx}R_{amz-ry}R_{amz-rz}$

Notes: T means translational constraint, and R means rotational constraint. The subscribes pmx, pmy and pmz indicate the PM local coordinate systems $O_{pmx}-X_{pmx}Y_{pmx}Z_{pmx}$, $O_{pmy}-X_{pmy}Y_{pmy}Z_{pmy}$ and $O_{pmz}-X_{pmz}Y_{pmz}Z_{pmz}$; and the subscribes amx, amy and amz indicate AM local coordinate systems $O_{amx}-X_{amx}Y_{amx}Z_{amx}$, $O_{amy}-X_{amy}Y_{amy}Z_{amy}$ and $O_{amz}-X_{amz}Y_{amz}Z_{amz}$, respectively. The subscripts -tx, -ty, -tz, -rx, -ry and -rz represent the directions along and about the three orthogonal axes of each coordinate system. For example, T_{pmx-tx} denotes the translational constraint along the X_{pmx}-axis of the coordinate system $O_{pmx}-X_{pmx}Y_{pmx}Z_{pmx}$, and R_{pmx-ry} represents the rotational constraint about the Y_{pmx}-axis of the coordinate system $O_{pmx}-X_{pmx}Y_{pmx}Z_{pmx}$.

2.　Synthesize the PMs and AMs based on the constraints selected in Step 1 above. In this paper, the PMs and AMs are designed using the freedom and constraint topology approach as shown in Figures 2 and 3. It can be seen that the synthesized PMs and AMs can be fabricated easily.

3.　Design the rigid stages, MS, ASs and BSs. Choose cubes as the MS and BSs, and the rigid stages of the AMs can also be used as the three ASs. Note that the exact dimensions of the MS, ASs and BSs can be ignored in this design step.

4.　Assemble the PMs, AMs, MS and BSs based on the coordinate systems, as shown in Figure 4a.

5.　Identify the final positions for the compliant modules and rigid stages. Using the position space identification method described in [18], the PMs and AMs can translate freely in any direction, and each of the PMs and AMs can also rotate about the X-axis of the local coordinate system, as shown in Figure 4b.The positions of the rigid stages, PMs and AMs, as illustrated in Figure 4a, are chosen as the final positions for the PMs and AMs due to the corresponding easily fabricated structure.

6.　Improve the motion performance of the XYZ CPM synthesized in Step 5. The CPI approach can ensure that the designed XYZ CPM in Step 5 has the motion characteristics of kinematic decoupling and actuation isolation. However, the parasitic rotations of the MS are not constrained well. Therefore, three identical redundant legs are added to reduce the parasitic rotations of the MS, as shown in Figure 5.

7.　Reduce the lost motion rate between the ASs and the MS. In order to do this, any two ASs associated with the same translation of the MS are rigidly linked, which can be seen in Figure 6a. Two rigidly-linked ASs always have the same motion displacements, because all rigid stages are assumed to be perfectly rigid, as stated in Section 2. Therefore, if one actuation force is exerted on any one of the two linked ASs, the two ASs will move together. Consequently, each translation of the MS is actuated by two ASs in opposite directions simultaneously, which can reduce the lost motion rates between the ASs and the MS. Note that the rigid linkages can also further decouple the primary translations of ASs from each other. In addition, the three rigid linkages can be made

of a material with high stiffness and small density, which can reduce the effect of the asymmetric configuration on the XYZ CPM.

8. Check if the XYZ CPM designed in Step 7 meets the design requirements. The synthesized XYZ CPM, as shown in Figure 6, has the desired characteristics, so it is the final design.
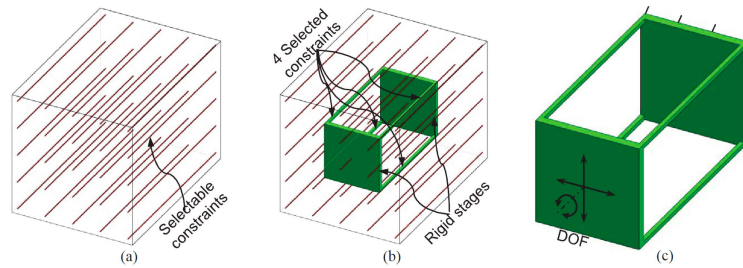

Figure 2. PM design based on the freedom and constraint topology approach: (**a**) the selectable constraints, (**b**) constraint selection and (**c**) the designed PM and its DOF.
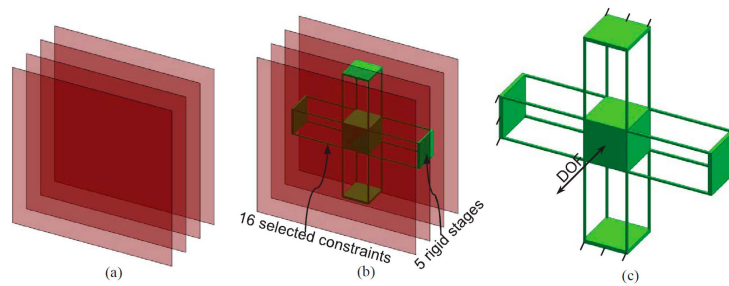

Figure 3. AM design based on the freedom and constraint topology approach: (**a**) the selectable constraints, (**b**) constraint selection and (**c**) the designed AM and its DOF.
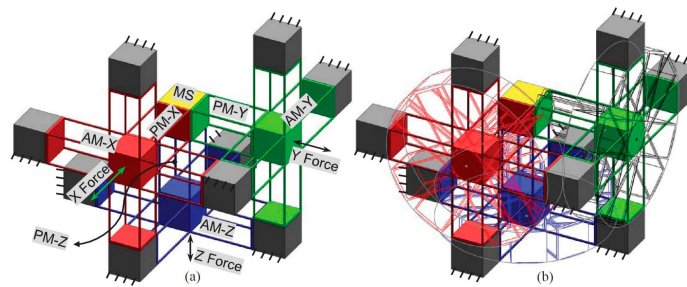
Figure 4. Assembly of the rigid stages and the compliant modules: (**a**) three-legged XYZ CPM assembled, based on the coordinate systems shown in Figure 1 and (**b**) illustration of some permitted positions of the PMs and AMs.
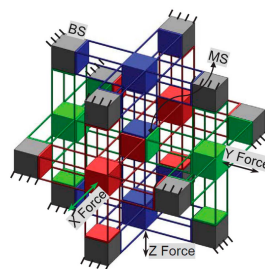
Figure 5. A fully symmetric design, obtained by adding three redundant legs to the XYZ CPM shown in Figure 4a.
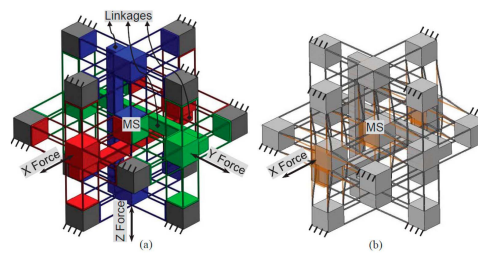
Figure 6. Final design of the XYZ CPM with three rigid linkages: (**a**) the final design and (**b**) the motion along the X-axis.

4. FEA-Result-Based Kinematic Analysis

In this section, the motion characteristics, including the cross-axis coupling rates, the lost motion rates, the parasitic rotations and the parasitic translations of the XYZ CPM are analyzed based on the FEA results. And the relations between the motion characteristics and the geometric parameters are studied. In addition, the comparison between the two XYZ CPMs with and without the rigid linkages, as shown in Figures 5 and 6 is also carried out.

The designed XYZ CPM, as shown in Figure 6, has an isotropic configuration (all the wire beams of the XYZ CPM are identical in dimension and material), so only the motion characteristics associated with one of the three orthogonal directions needs to be analyzed. In this paper, the motion characteristics associated with the X-axis translation is studied. The rotational stiffness of the ASs is larger than those of the MS, due to introducing the three rigid linkages. So the parasitic rotations of the ASs should not be larger than the parasitic rotations of the MS. Therefore, the parasitic rotations of the ASs are not analyzed in this case. As a result, only the primary translations of the MS and the AS-X, the parasitic rotations of the MS, and the parasitic translations of the AS-X are studied in this case. Additionally, in this paper, the displacements and lengths are normalized by the beam length L, the translational forces are normalized by EI/L^2, and the rotational forces are normalized by EI/L, where E is the Young's modulus of the material, and I is the second moment of area of the beam [29].

For the FEA model, assume that E = 69,000 MPa, v = 0.33, and the normalized motion range per axis is limited to $\pm5\%L$ which can be considered as a medium-large motion range compared with the beam length [29]. Moreover, the commercial software, COMSOL MULTIPHYSICS (COMSOL Group, Stockholm, Sweden), is selected for the nonlinear FEA simulations, using the 10-node tetrahedral element and fine meshing technology. In addition, the three actuations are applied on the surface centers of the three cubic ASs, respectively, as shown in Figure 6. Additionally, each of the three actuation points is the motion reference point of the AS in the FEA simulations, whose motion is regarded as the motion of the AS. Similarly, the center point of the cubic MS is defined as the motion reference point of the MS.

The main geometric parameters of the XYZ CPM are the beam length L, the beam thickness T and the width W of the identical cubes, which can be analyzed in the following two dimensionless parameters: beam's slenderness ratio λ_b (in this paper, $\lambda_b = L/T$) and the ratio, w, of the W to the L (w is actually the normalized width of the identical cubes, which equals to W/L). In order to estimate the effects of the two dimensionless parameters on the motion characteristics, a series of values are selected for the two dimensionless parameters, λ_b and w, in the FEA model.

In order to achieve a several-millimeter motion range, the beam length L should be up to dozens of millimeters (as mentioned above, the motion range per axis equals to $\pm5\%L$). So it is appropriate to select 20, 30, 40, 50, 60, 70, 80, 90 and 100 mm as the beam length, respectively. For these beam lengths, 1 mm beam thickness and 20 mm width are appropriate. Based on the above selected dimension, λ_b varies from 20 to 100. For each of the values of λ_b, FEA simulation is carried out, under the following actuation condition: The normalized X-axis actuation displacement, $\xi_{asx\text{-}tx}$, varies from -0.05 to $+0.05$, and the other two normalized actuation displacements, $\xi_{asy\text{-}tx}$ and $\xi_{asz\text{-}tx}$, are both 0.05. In this actuation condition, the cross-axis coupling rate regarding the MS's X-axis translation, the lost

motion rate along the X-axis, the parasitic rotations of the MS about the Y- and Z-axes, and the parasitic translations of the AS-X along the Y- and Z-axes can reach their maximum values.

The FEA results are shown in Figure 7. With λ_b changing from 20 to 100, it can be seen that: (a) the maximum cross-axis coupling rate, in terms of the MS's X-axis translation, reduces from 0.86% to 0.32%, as shown in Figure 7a; (b) the maximum X-axis lost motion rate varies from 1.20% to 0.60%, as shown in Figure 7b; (c) the parasitic rotation of the MS about the X-axis shows a highly discontinuous behavior responding to the slenderness ratio conditions, which are in the order of 10^{-6} rad, as shown in Figure 7c; (d) the maximum parasitic rotation of the MS about the Y- or Z-axis increases slightly, but is still in the order of 10^{-5}, as shown in Figure 7d,e; and (e) the normalized parasitic translations of the AS-X along the Y- and Z-axes decrease from about 1.5×10^{-4} to 0.76×10^{-4}, as shown in Figure 7f,g. In the condition of increasing the value of λ_b, the FEA results reveal that the cross-axis coupling rate, the lost motion rate and the parasitic translations decrease, but the parasitic rotations increase slightly. It can also be seen that the obtained cross-axis coupling rate, lost motion rate, parasitic rotations and parasitic translations are reduced compared with the XYZ CPM proposed in [9], for all the values of λ_b.

Compared with the effect of λ_b under the same actuation condition, the effect of *w* on the motion characteristics of the XYZ CPM is negligible, which can be seen from the FEA results shown in Table 3 (when *L* = 30 mm). Particularly, the cross-axis coupling rate and the lost motion rate do not change, when the *w* are assigned 1/3, 2/3 and 1, respectively. The parasitic rotations decrease slightly when increasing the *w* value.

The comparison of the motion characteristics of the two XYZ CPMs with and without the rigid linkages, as shown in Figures 5 and 6 is also conducted in this section. When λ_b = 30 and *w* = 2/3, the comparison of the motion characteristics of the two XYZ CPMs is demonstrated in Figure 8. The FEA results illustrate that: (a) the cross-axis coupling rate, the lost motion rate and the parasitic rotations of the XYZ CPM with the rigid linkages are much smaller than corresponding ones of the XYZ CPM without the rigid linkages, respectively; and (b) the AS-X of the XYZ CPM with the rigid linkages has slightly larger normalized parasitic translations, which are, however, in the order of 10^{-4} and less than 0.23% of the primary translation of the AS-X. For any one of the two XYZ CPMs with and without the rigid linkages, the parasitic translations of the AS-X along the Y- and Z-axes mainly arise from the actuation forces along the Y- and Z-axes, respectively. The parasitic translations of the AS-X of the XYZ CPM without the rigid linkages along the Y- and Z-axes are slightly smaller than those of the XYZ CPM with the rigid linkages, probably because, for a certain displacement of the AS-X, the XYZ CPM without the rigid linkages needs a smaller actuation force along the X-axis.
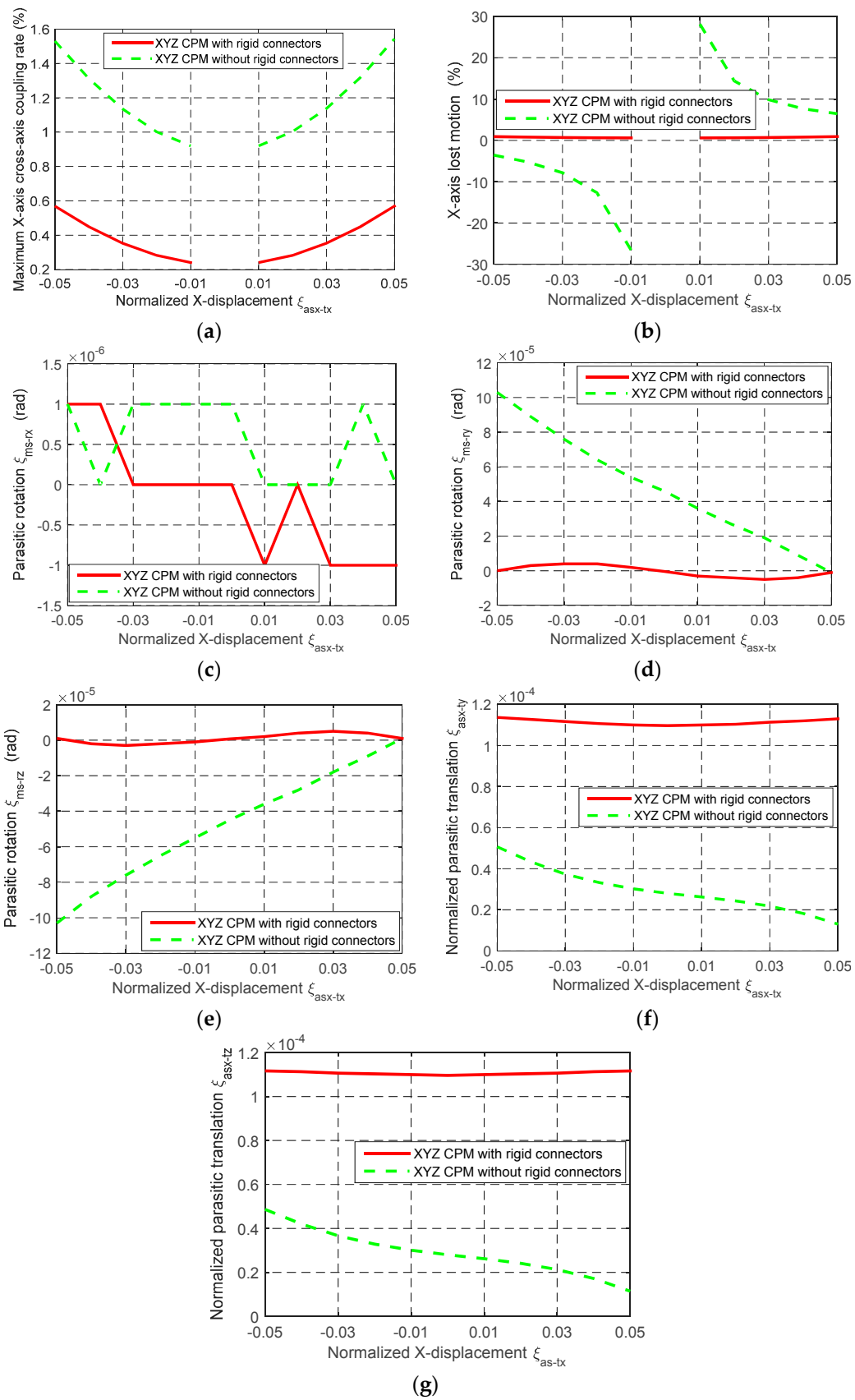
Table 3. The variation of the motion characteristics of the XYZ CPM with the rigid-cube width *w*.

AS-X X-Translation, $\xi_{asx\text{-}tx}$		−0.05	−0.03	−0.01	0.01	0.03	0.05
Cross-axis coupling rate (%)	$w = 1/3$	0.57	0.35	0.24	0.24	0.35	0.57
	$w = 2/3$	0.57	0.35	0.24	0.24	0.35	0.57
	$w = 1$	0.57	0.35	0.24	0.24	0.35	0.57
Lost motion rate (%)	$w = 1/3$	0.90	0.70	0.59	0.59	0.70	0.90
	$w = 2/3$	0.90	0.70	0.59	0.60	0.70	0.90
	$w = 1$	0.90	0.70	0.59	0.60	0.70	0.90
MS X-rotation, $\xi_{ms\text{-}rx}$, (rad)	$w = 1/3$	0.00×10^{0}	0.00×10^{0}	-1.00×10^{-6}	-1.00×10^{-6}	0.00×10^{0}	-1.00×10^{-6}
	$w = 2/3$	1.00×10^{-6}	0.00×10^{0}	0.00×10^{0}	-1.00×10^{-6}	-1.00×10^{-6}	-1.00×10^{-6}
	$w = 1$	-3.00×10^{-6}	-2.00×10^{-6}	-1.00×10^{-6}	-1.00×10^{-6}	-1.00×10^{-6}	-1.00×10^{-6}
MS Y-rotation, $\xi_{ms\text{-}ry}$, (rad)	$w = 1/3$	0.00×10^{0}	6.00×10^{-6}	3.00×10^{-6}	-3.00×10^{-6}	-6.00×10^{-6}	0.00×10^{0}
	$w = 2/3$	0.00×10^{0}	4.00×10^{-6}	2.00×10^{-6}	-3.00×10^{-6}	-5.00×10^{-6}	-1.00×10^{-6}
	$w = 1$	0.00×10^{0}	4.00×10^{-6}	2.00×10^{-6}	-1.00×10^{-6}	-2.00×10^{-6}	2.00×10^{-6}
MS Z-rotation, $\xi_{ms\text{-}rz}$, (rad)	$w = 1/3$	0.00×10^{0}	-5.00×10^{-6}	-3.00×10^{-6}	3.00×10^{-6}	5.00×10^{-6}	0.00×10^{0}
	$w = 2/3$	1.00×10^{-6}	-3.00×10^{-6}	-1.00×10^{-6}	2.00×10^{-6}	5.00×10^{-6}	1.00×10^{-6}
	$w = 1$	1.00×10^{-6}	-4.00×10^{-6}	-2.00×10^{-6}	1.00×10^{-6}	3.00×10^{-6}	$0.00 \times 10^{0\circ}$
AS-X Y-translation, $\xi_{asx\text{-}ty}$	$w = 1/3$	1.12×10^{-4}	1.11×10^{-4}	1.09×10^{-4}	1.09×10^{-4}	1.10×10^{-4}	1.11×10^{-4}
	$w = 2/3$	1.14×10^{-4}	1.12×10^{-4}	1.10×10^{-4}	1.10×10^{-4}	1.11×10^{-4}	1.13×10^{-4}
	$w = 1$	1.11×10^{-4}	1.10×10^{-4}	1.09×10^{-4}	1.09×10^{-4}	1.10×10^{-4}	1.11×10^{-4}
AS-X Z-translation, $\xi_{asx\text{-}tz}$	$w = 1/3$	1.12×10^{-4}	1.11×10^{-4}	1.10×10^{-4}	1.10×10^{-4}	1.11×10^{-4}	1.12×10^{-4}
	$w = 2/3$	1.12×10^{-4}	1.11×10^{-4}	1.10×10^{-4}	1.10×10^{-4}	1.11×10^{-4}	1.12×10^{-4}
	$w = 1$	1.11×10^{-4}	1.10×10^{-4}	1.09×10^{-4}	1.09×10^{-4}	1.10×10^{-4}	1.11×10^{-4}
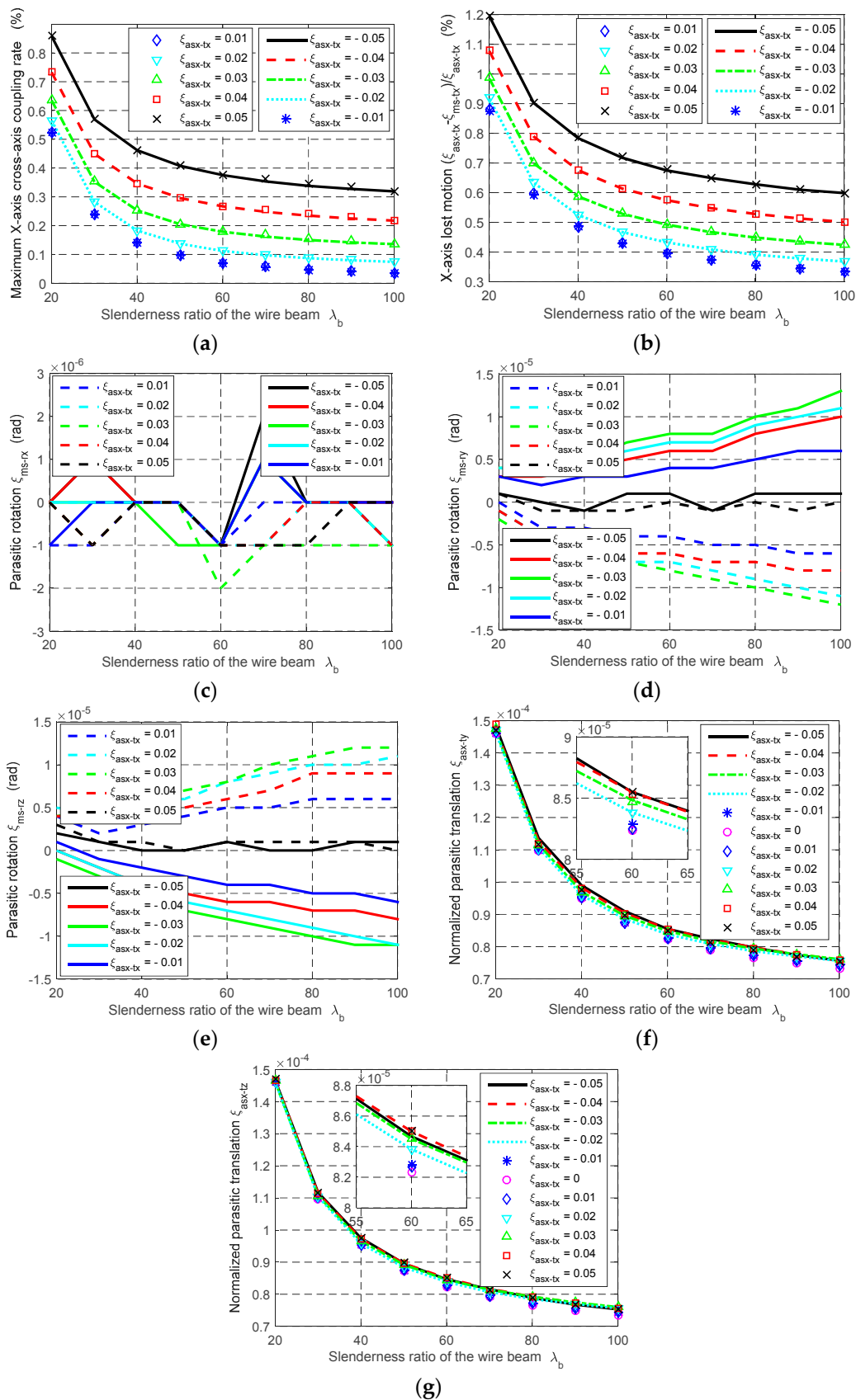
Figure 7. The variation of the motion characteristics of the XYZ CPM with the beam slenderness ratios λ_b: (**a**) Cross-axis coupling rate in terms of the X-axis primary translation of the MS, (**b**) lost motion rate along the X-axis, (**c**–**e**) parasitic rotations of the MS about the X-, Y- and Z-axes, respectively and (**f**–**g**) parasitic translations of the AS along the Y- and Z-axes, respectively.

Figure 8. The comparison of the motion characteristics of the two XYZ CPMs with and without the rigid linkages, as shown in Figures 5 and 6 respectively: (**a**) Cross-axis coupling rate in terms of the X-axis primary translation of the MS, (**b**) lost motion rate along the X-axis, (**c**–**e**) parasitic rotations of the MS about the X-, Y- and Z-axes; respectively and (**f**–**g**) parasitic translations of the AS along the Y- and Z-axes, respectively.

5. Analytical Modeling

The motion characteristics of the XYZ CPM, as shown in Figure 6, are predicted based on the FEA results, and the relations between the motion characteristics and the main geometric parameters are studied as well. In this section, the nonlinear analytical model of the XYZ CPM is derived, which can be used to predict the force-displacement relationship, and to estimate the actuation stiffness, before conducting FEA simulations and experimental tests. As observed in Section 4, the parasitic rotations and the parasitic translations are much smaller than the primary translations. Therefore, it is appropriate to ignore the effects of the parasitic motion on the analytical models of the primary translations.

Each PM of the XYZ CPM can be referred to as a four-beam compliant module (FBCM) as shown in Figure 9, and each AM of the XYZ CPM can be regarded as the parallel combination of four FBCMs. Therefore, the motions of the XYZ CPM are performed through the deformation of the FBCMs in the XYZ CPM, so the modeling of the FBCM is carried out before modeling the complete XYZ CPM.
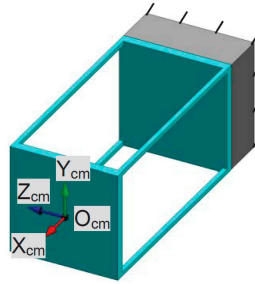

Figure 9. An FBCM and its coordinate system.

The analytical model of the FBCM can be found in [30,31], which can be rewritten as Equations (1)–(3).

$$\zeta_{\text{cm-tx}} = -\frac{1680\left(5\xi_{\text{cm-tx}} + 3\left(\xi_{\text{cm-ty}}^2 + \xi_{\text{cm-tz}}^2\right)\right)}{175t^2 + 3\xi_{\text{cm-ty}}^2 + 3\xi_{\text{cm-tz}}^2} \tag{1}$$

$$\zeta_{\text{cm-ty}} = -\frac{48\xi_{\text{cm-ty}}\left(175t^2 + 210\xi_{\text{cm-tx}} + 129\xi_{\text{cm-ty}}^2 + 129\xi_{\text{cm-tz}}^2\right)}{175t^2 + 3\xi_{\text{cm-ty}}^2 + 3\xi_{\text{cm-tz}}^2} \tag{2}$$

$$\zeta_{\text{cm-tz}} = -\frac{48\xi_{\text{cm-tz}}\left(175t^2 + 210\xi_{\text{cm-tx}} + 129\xi_{\text{cm-ty}}^2 + 129\xi_{\text{cm-tz}}^2\right)}{175t^2 + 3\xi_{\text{cm-ty}}^2 + 3\xi_{\text{cm-tz}}^2} \tag{3}$$

where t is normalized thickness of the beam. $\xi_{\text{cm-tx}}$, $\xi_{\text{cm-ty}}$ and $\xi_{\text{cm-tz}}$ are the translational displacements of the FBCM's output stage along the X_{cm}-, Y_{cm}- and Z_{cm}-axes, respectively. $\zeta_{\text{cm-tx}}$, $\zeta_{\text{cm-ty}}$ and $\zeta_{\text{cm-tz}}$ are the reaction forces along the X_{cm}-, Y_{cm}- and Z_{cm}-axes, respectively, which are produced by the FBCM due to the deformation of the beams in the FBCM. Note that the rotations of the FBCM about the X_{cm}-, Y_{cm}- and Z_{cm}-axes are not taken into account, because the rotations of the FBCM in the XYZ CPM system are negligible compared with the translations, as analyzed in Section 4.

According to the analytical model, an FBCM can be regarded as a three-dimension translational spring. The complete XYZ CPM can be modeled based on the analytical model of the three-dimension translational spring. As already mentioned, the motion performance of the XYZ CPM along the X_{ms}-, Y_{ms}- and Z_{ms}-axes are identical (O_{ms}-$X_{\text{ms}}Y_{\text{ms}}Z_{\text{ms}}$ are the global coordinate system in this section). Therefore, only the primary translations along one of the three directions need to be studied. In this paper, the derivation of the force-displacement relationship, associated with only the translations along the X_{ms}-axis, is detailed. Given any displacements, $\xi_{\text{asy-tx}}$ and $\xi_{\text{asz-tx}}$, of the AS-Y and AS-Z, respectively, the XYZ CPM can be simplified to the model shown in Figure 10 if only the force-displacement relationship in X_{m}-axis is concerned.
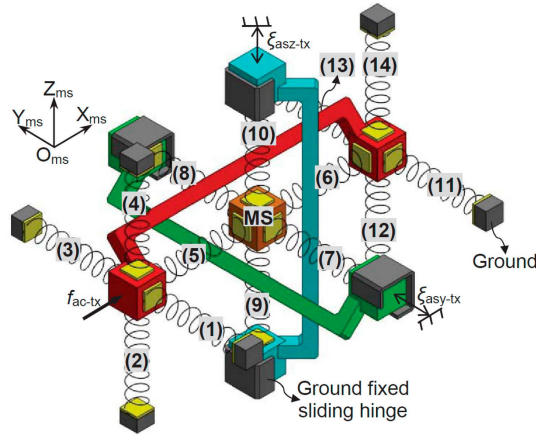
Figure 10. Demonstration of the rigid stages and FBCMs in the XYZ CPM system associated with only the X_{ms}-axis translation (AS-Xs and their rigid linkage are red in color, AS-Ys and their rigid linkage are green in color, and AS-Zs and their rigid linkage are blue in color).

Assume that the lost motions along the X_{ms}-, Y_{ms}- and Z_{ms}-axes are δ_x, δ_y and δ_z, respectively, which can be written as shown in Equation (4).

$$\delta_x = \xi_{asx\text{-}tx} - \xi_{ms\text{-}tx}, \ \delta_y = \xi_{asy\text{-}tx} - \xi_{ms\text{-}ty} \text{ and } \delta_z = \xi_{asz\text{-}tx} - \xi_{ms\text{-}tz} \tag{4}$$

where $\xi_{ms\text{-}tx}$, $\xi_{ms\text{-}ty}$, $\xi_{ms\text{-}tz}$, $\xi_{asx\text{-}tx}$, $\xi_{asy\text{-}tx}$ and $\xi_{asz\text{-}tx}$ are the primary translations of the MS and ASs, as defined in Section 1. The model, as shown in Figure 10, contains 14 FBCMs, which are termed as FBCM-1 to FBCM-14, respectively. If all the parasitic rotations and parasitic translations of the XYZ CPM are ignored, the deformation displacements of each of the FBCMs can be obtained easily according to the primary translations and lost motions. Additionally, the reaction forces of the FBCMs can also be calculated based on Equation (1). Taking the FBCM-1 as an example, the FBCM-1 is linked to the AS-X, so the deformation displacements of the FBCM-1 can be derived from the motion displacements of the AS-X. If ignoring all the parasitic rotations and parasitic translations of the AS-X, the deformation displacements of the FBCM-1 equal to $\xi_{asx\text{-}tx}$, zero and zero along the X_{ms}-, Y_{ms}- and Z_{ms}-axes, respectively. Therefore, the reaction force, ζ_a, of the FBCM-1 along the X_{ms}-axis can be obtained, as shown in Equation (5), via substituting the deformation displacements of the FBCM-1 into Equations (2) or (3). Note that when substituting the deformation displacements into Equation (2), $\xi_{cm\text{-}tx}$, $\xi_{cm\text{-}ty}$ and $\xi_{cm\text{-}tz}$ in Equation (2) equal to zero, $\xi_{asx\text{-}tx}$ and zero, respectively; when substituting the deformation displacements into Equation (3), $\xi_{cm\text{-}tx}$, $\xi_{cm\text{-}ty}$ and $\xi_{cm\text{-}tz}$ in Equation (3) equal to zero, zero and ξ_{asx-tx}, respectively. Similarly, the reaction force of the FBCM-2, FBCM-3, FBCM-4, FBCM-11, FBCM-12, FBCM-13 or FBCM-14, to the AS-X along the X_{ms}-axis, can also be obtained as shown in Equation (5). Additionally, the reaction forces of the FBCM-5, FBCM-6, FBCM-7, FBCM-8, FBCM-9 and FBCM-10, to the MS along the X_{ms}-axis, can be derived in Equations (6)–(11), respectively, which are represented as ζ_b, ζ_c, ζ_d, ζ_e, ζ_f and ζ_g.

$$\zeta_a = -\frac{48\xi_{asx\text{-}tx}\left(129\xi_{asx\text{-}tx}^2 + 175t^2\right)}{3\xi_{asx\text{-}tx}^2 + 175t^2} \tag{5}$$

$$\zeta_b = \frac{1680\left(3\left(\xi_{ms\text{-}ty}^2 + \xi_{ms\text{-}tz}^2\right) - 5\delta_x\right)}{3\xi_{ms\text{-}ty}^2 + 3\xi_{ms\text{-}tz}^2 + 175t^2} \tag{6}$$

$$\zeta_c = -\frac{1680\left(3\left(\xi_{ms\text{-}ty}^2 + \xi_{ms\text{-}tz}^2\right) - 5\delta_x\right)}{3\xi_{ms\text{-}ty}^2 + 3\xi_{ms\text{-}tz}^2 + 175t^2} \tag{7}$$

$$\zeta_d = -\frac{48\xi_{ms\text{-}tx}\left(-210\delta_y + 129\xi_{ms\text{-}tx}^2 + 129\xi_{ms\text{-}tz}^2 + 175t^2\right)}{3\xi_{ms\text{-}tx}^2 + 3\xi_{ms\text{-}tz}^2 + 175t^2} \tag{8}$$

$$\zeta_e = -\frac{48\xi_{ms\text{-}tx}\left(210\delta_y + 129\xi_{ms\text{-}tx}^2 + 129\xi_{ms\text{-}tz}^2 + 175t^2\right)}{3\xi_{ms\text{-}tx}^2 + 3\xi_{ms\text{-}tz}^2 + 175t^2} \tag{9}$$

$$\zeta_f = -\frac{48\xi_{ms\text{-}tx}\left(-210\delta_z + 129\xi_{ms\text{-}ty}^2 + 129\xi_{ms\text{-}tx}^2 + 175t^2\right)}{3\xi_{ms\text{-}ty}^2 + 3\xi_{ms\text{-}tx}^2 + 175t^2} \tag{10}$$

$$\zeta_g = -\frac{48\xi_{ms\text{-}tx}\left(210\delta_z + 129\xi_{ms\text{-}ty}^2 + 129\xi_{ms\text{-}tx}^2 + 175t^2\right)}{3\xi_{ms\text{-}ty}^2 + 3\xi_{ms\text{-}tx}^2 + 175t^2} \tag{11}$$

When the MS is at static equilibrium, all the reaction forces on the MS along the X_{ms}-axis should be balanced, so Equation (12) can be obtained. Substituting Equations (6)–(11) into Equation (12), Equation (13) can be derived. Furthermore, the actuation force, $f_{ac\text{-}tx}$, should equal to the sum of the reaction forces of all the FBCMs except FBCM-5 and FBCM-6, along the X_{ms}-axis. Therefore, the relationship between the actuation force $f_{ac\text{-}tx}$ and the primary translations of the MS can be obtained, as shown in Equation (14).

$$\zeta_b + \zeta_c + \zeta_d + \zeta_e + \zeta_f + \zeta_g = 0 \tag{12}$$

$$\delta_x = \frac{2\xi_{ms\text{-}tx}\left(3\xi_{ms\text{-}ty}^2 + 3\xi_{ms\text{-}tz}^2 + 175t^2\right)\left(3\xi_{ms\text{-}tx}^2\left(129\xi_{ms\text{-}ty}^2 + 129\xi_{ms\text{-}tz}^2 + 7700t^2\right) + 175\left(66t^2\xi_{ms\text{-}tz}^2 + 175t^4\right)\right)}{175\left(3\xi_{ms\text{-}tx}^2 + 3\xi_{ms\text{-}ty}^2 + 175t^2\right)\left(3\xi_{ms\text{-}tx}^2 + 3\xi_{ms\text{-}tz}^2 + 175t^2\right)} +$$
$$\frac{6\xi_{ms\text{-}tx}\left(3\xi_{ms\text{-}ty}^2 + 3\xi_{ms\text{-}tz}^2 + 175t^2\right)\left(\xi_{ms\text{-}ty}^2\left(129\xi_{ms\text{-}tz}^2 + 3850t^2\right) + 129\xi_{ms\text{-}tx}^4\right)}{175\left(3\xi_{ms\text{-}tx}^2 + 3\xi_{ms\text{-}ty}^2 + 175t^2\right)\left(3\xi_{ms\text{-}tx}^2 + 3\xi_{ms\text{-}tz}^2 + 175t^2\right)} \tag{13}$$

$$f_{ac\text{-}tx} = 96\xi_{ms\text{-}tx}\left(\frac{516\xi_{ms\text{-}tx}^2 + 700t^2}{3\xi_{ms\text{-}tx}^2 + 175t^2} + \frac{129\xi_{ms\text{-}tx}^2 + 129\xi_{ms\text{-}ty}^2 + 175t^2}{3\xi_{ms\text{-}tx}^2 + 3\xi_{ms\text{-}ty}^2 + 175t^2} + \frac{129\xi_{ms\text{-}tx}^2 + 129\xi_{ms\text{-}tz}^2 + 175t^2}{3\xi_{ms\text{-}tx}^2 + 3\xi_{ms\text{-}tz}^2 + 175t^2}\right) \tag{14}$$

Similarly, the lost motions along the Y_{ms}- and Z_{ms}-axes and the force-displacement relationships associated with the actuation forces, $f_{ac\text{-}ty}$ and $f_{ac\text{-}tz}$, can be derived as shown in Equations (15)–(18). Note that the actuation forces, $f_{ac\text{-}ty}$ and $f_{ac\text{-}tz}$, are applied on the AS-Y and AS-Z, respectively.

$$\delta_y = \frac{2\xi_{ms\text{-}ty}\left(3\xi_{ms\text{-}tx}^2 + 3\xi_{ms\text{-}tz}^2 + 175t^2\right)\left(3\xi_{ms\text{-}ty}^2\left(129\xi_{ms\text{-}tx}^2 + 129\xi_{ms\text{-}tz}^2 + 7700t^2\right) + 175\left(66t^2\xi_{ms\text{-}tz}^2 + 175t^4\right)\right)}{175\left(3\xi_{ms\text{-}tx}^2 + 3\xi_{ms\text{-}ty}^2 + 175t^2\right)\left(3\xi_{ms\text{-}ty}^2 + 3\xi_{ms\text{-}tz}^2 + 175t^2\right)} +$$
$$\frac{6\xi_{ms\text{-}ty}\left(3\xi_{ms\text{-}tx}^2 + 3\xi_{ms\text{-}tz}^2 + 175t^2\right)\left(\xi_{ms\text{-}tx}^2\left(129\xi_{ms\text{-}tz}^2 + 3850t^2\right) + 129\xi_{ms\text{-}ty}^4\right)}{175\left(3\xi_{ms\text{-}tx}^2 + 3\xi_{ms\text{-}ty}^2 + 175t^2\right)\left(3\xi_{ms\text{-}ty}^2 + 3\xi_{ms\text{-}tz}^2 + 175t^2\right)} \tag{15}$$

$$f_{ac\text{-}ty} = 96\xi_{ms\text{-}ty}\left(\frac{516\xi_{ms\text{-}ty}^2 + 700t^2}{3\xi_{ms\text{-}ty}^2 + 175t^2} + \frac{129\xi_{ms\text{-}tx}^2 + 129\xi_{ms\text{-}ty}^2 + 175t^2}{3\xi_{ms\text{-}tx}^2 + 3\xi_{ms\text{-}ty}^2 + 175t^2} + \frac{129\xi_{ms\text{-}ty}^2 + 129\xi_{ms\text{-}tz}^2 + 175t^2}{3\xi_{ms\text{-}ty}^2 + 3\xi_{ms\text{-}tz}^2 + 175t^2}\right) \tag{16}$$

$$\delta_z = \frac{2\xi_{ms\text{-}tz}\left(3\xi_{ms\text{-}tx}^2 + 3\xi_{ms\text{-}ty}^2 + 175t^2\right)\left(3\xi_{ms\text{-}tz}^2\left(129\xi_{ms\text{-}tx}^2 + 129\xi_{ms\text{-}ty}^2 + 7700t^2\right) + 175\left(66t^2\xi_{ms\text{-}tx}^2 + 175t^4\right)\right)}{175\left(3\xi_{ms\text{-}ty}^2 + 3\xi_{ms\text{-}tz}^2 + 175t^2\right)\left(3\xi_{ms\text{-}tx}^2 + 3\xi_{ms\text{-}tz}^2 + 175t^2\right)} +$$
$$\frac{6\xi_{ms\text{-}tz}\left(3\xi_{ms\text{-}tx}^2 + 3\xi_{ms\text{-}ty}^2 + 175t^2\right)\left(\xi_{ms\text{-}ty}^2\left(129\xi_{ms\text{-}tx}^2 + 3850t^2\right) + 129\xi_{ms\text{-}tz}^4\right)}{175\left(3\xi_{ms\text{-}ty}^2 + 3\xi_{ms\text{-}tz}^2 + 175t^2\right)\left(3\xi_{ms\text{-}tx}^2 + 3\xi_{ms\text{-}tz}^2 + 175t^2\right)} \tag{17}$$

$$f_{ac\text{-}tz} = 96\xi_{ms\text{-}tz}\left(\frac{516\xi_{ms\text{-}tz}^2 + 700t^2}{3\xi_{ms\text{-}tz}^2 + 175t^2} + \frac{129\xi_{ms\text{-}ty}^2 + 129\xi_{ms\text{-}tz}^2 + 175t^2}{3\xi_{ms\text{-}ty}^2 + 3\xi_{ms\text{-}tz}^2 + 175t^2} + \frac{129\xi_{ms\text{-}tx}^2 + 129\xi_{ms\text{-}tz}^2 + 175t^2}{3\xi_{ms\text{-}tx}^2 + 3\xi_{ms\text{-}tz}^2 + 175t^2}\right) \tag{18}$$

Based on Equations (14)–(18), the actuation forces, $f_{ac\text{-}tx}$, $f_{ac\text{-}ty}$ and $f_{ac\text{-}tz}$, and the lost motions, δ_x, δ_y and δ_z, can be obtained when specific translational displacements of the MS, $\xi_{ms\text{-}tx}$, $\xi_{ms\text{-}ty}$ and

$\xi_{ms\text{-}tz}$, are required. Furthermore, the primary translational displacements of the ASs, $\xi_{asx\text{-}tx}$, $\zeta_{asy\text{-}tx}$ and $\xi_{asz\text{-}tx}$, can also be obtained according to Equation (4).

The derived analytical models of the primary translations of the MS and ASs are applicable for any geometric dimension and material. When $L = 30$ mm, $W = 20$ mm, $T = 1$ mm, $E = 69{,}000$ MPa and $v = 0.33$, the analytical and FEA results of the X_{ms}-axis actuation force and the X_{ms}-axis lost motion, can be seen in Figures 11 and 12 under the following three actuation conditions: (a) $\xi_{asx\text{-}tx}$ varies from -0.05 to $+0.05$, $\xi_{asy\text{-}tx} = 0$ and $\xi_{asz\text{-}tx} = 0$; (b) $\xi_{asx\text{-}tx}$ varies from -0.05 to $+0.05$, $\xi_{asy\text{-}tx} = 0.05$ and $\xi_{asz\text{-}tx} = 0$; and (c) $\xi_{asx\text{-}tx}$ varies from -0.05 to $+0.05$, $\xi_{asy\text{-}tx} = 0.05$ and $\xi_{asz\text{-}tx} = 0.05$. Figure 11 shows that the analytical results and the FEA results of the X_{ms}-axis actuation force match very well, with less than 2% difference. Figure 12 illustrates that the maximum difference between the analytical results and the FEA results of the X_{ms}-axis lost motion rate is less than 5.8%. It can be predicted that the analytical model of the MS's primary translations should match the FEA model as well, according to Equation (4).

As studied in Section 4, the cross-axis coupling rate and the lost motion rate of the XYZ CPM along the X_{ms}-axis are less than 0.38% and 0.68%, respectively, when $\lambda_b = 60$ and $w = 1/3$. Therefore, along one axis, the primary translations of the MS and the AS are almost decoupled from the primary translations of the MS and the ASs along the other two axes. However, the X_{ms}-axis actuation forces, when $\xi_{asy\text{-}tx} \neq 0$ and $\xi_{asz\text{-}tx} \neq 0$, slightly deviate from the X_{ms}-axis actuation force when $\xi_{asy\text{-}tx} = 0$ and $\xi_{asz\text{-}tx} = 0$, as shown in Figure 11. The deviation does not arise from the cross-axis coupling, but from the increase of the actuation stiffness along the X_{ms}-axis due to the exerted actuation displacements, $\xi_{asy\text{-}tx}$ and $\xi_{asz\text{-}tx}$, along the Y_{ms}- and Z_{ms}-axes. The actuation stiffness along the three axes can be predicted by the derived analytical models, and the actuators can be selected based on the actuation stiffness.
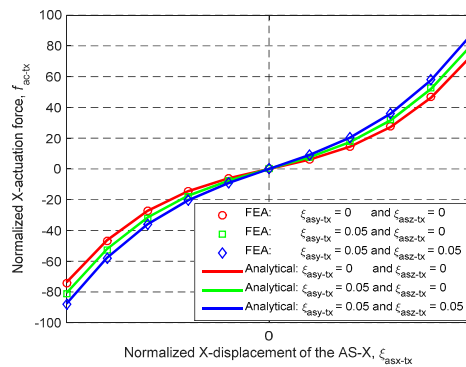
Figure 11. Analytical result and FEA result comparison regarding the relationship between the normalized X_{ms}-axis primary translation of the AS-X and the normalized X_{ms}-axis actuation force under the different conditions.
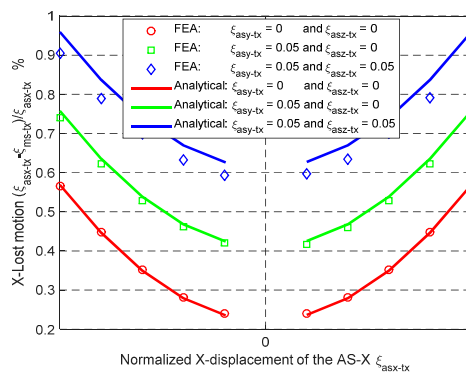

Figure 12. Analytical result and FEA result comparison regarding the relationship between the normalized X_{ms}-axis primary translation of the AS-X and the X_{ms}-axis lost motion under the different conditions.

6. Fabrication Considerations

The proposed new XYZ CPM has excellent motion performance. However, the MS of the XYZ CPM is located at the center of the whole structure. In order to fabricate the proposed XYZ CPM, two practical designs, design-I and design-II, of the proposed XYZ CPM are presented in this section.

Design-I, as shown in Figure 13a, has an output platform, which is connected to the MS with an output platform linkage. Therefore, the motion of the MS can be transmitted to the output platform, *i.e.*, the output platform can translate in the three orthogonal directions under the actuation of the three actuators. Design-I is obtained by assembling the following basic accessories, as shown in Figure 13b–h, using bolts and nuts: compliant beam component with larger spanning size, compliant beam component with smaller spanning size, rigid cube linkage, rigid cube, washer, output platform linkage, and output platform. The two types of compliant beam components have different spanning size in order to prevent the interference between them in design-I. Both types of the compliant components are placed symmetrically in the practical design, so the small difference in the spanning size (the difference equals to twice the beam's thickness) has a negligible effect on the motion characteristic. Each of the accessories has mounting holes which are used to assemble the accessory to design-I. The compliant beam components can be obtained through cutting a thin plate using a CNC milling machine, and the other basic accessories can also be fabricated using a CNC milling machine. The output platform is the last assembled accessory, and the other assembling steps are demonstrated in Figure 14.
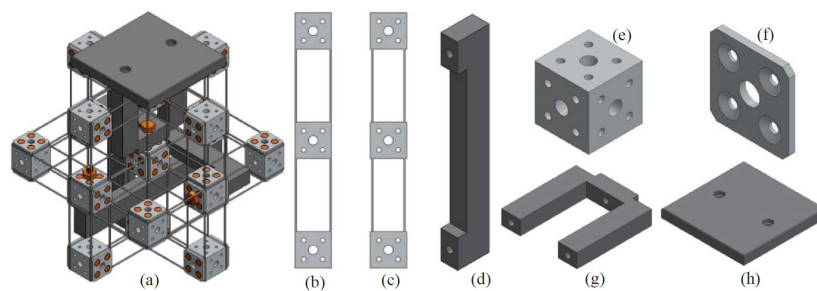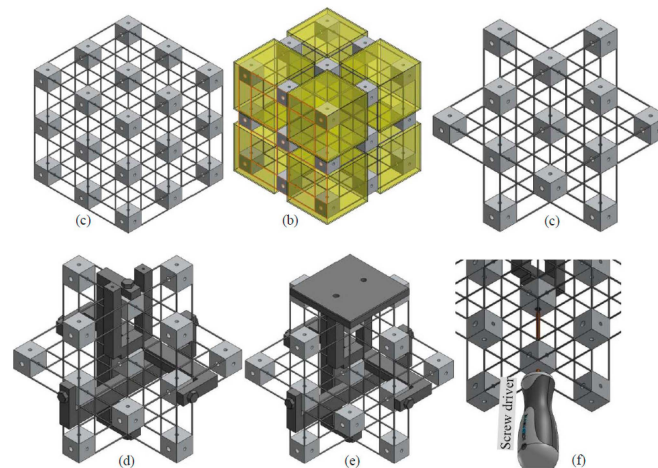

Figure 13. Practical design-I and its assembling accessories: (**a**) practical design-I, (**b**) compliant beam component with larger spanning size, (**c**) compliant beam component with smaller spanning size, (**d**) rigid cube linkage, (**e**) rigid cube, (**f**) washer, (**g**) output platform linkage and (**h**) output platform.
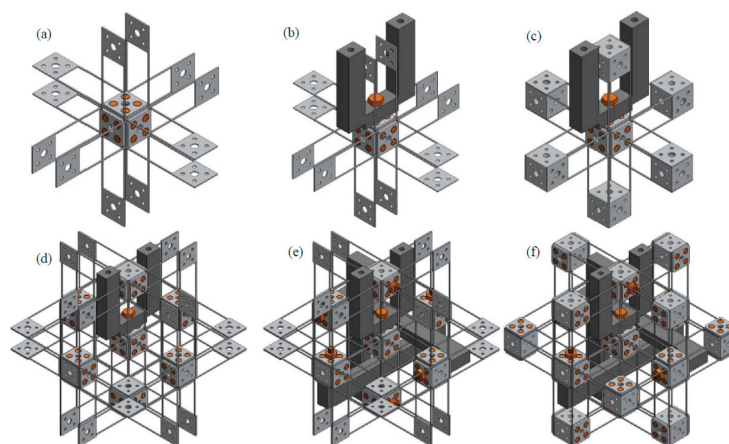
Figure 14. Assembling process of the design-I: (**a**) MS and its connected compliant beam components assembly, (**b**) output platform linkage assembly, (**c**) ASs assembly, (**d**) AS connected compliant beam components assembly, (**e**) rigid cube linkage assembly and (**f**) other rigid cubes assembly.

Design-I has only seven different basic assembling accessories. Additionally, each of the basic assembling accessories can be fabricated easily. When one of the basic assembling accessories is broken, it is convenient to replace it with a new one. Moreover, different materials can be selected for the seven basic assembling accessories. For example, one can select Al6061 for the compliant beam components, select stainless steel for the rigid cubes and cube linkages, and select Polycarbonate for the output platform and its linkage.

All of the rigid cubes and the compliant beam components can also be fabricated as a monolithic model, as shown in Figure 15a. The model can be fabricated through cutting along the three orthogonal directions, using electrical discharge machining technologies. If all the beams connecting to the eight vertex cubes of the model shown in Figure 15b are cut off, the model shown in Figure 15c can be obtained. Note that the associated rigid cubes should be fixed when cutting a compliant beam from them. The model, as shown in Figure 15c, is the key part of the practical design-II. Figure 15d–e illustrate the assembling of the output platform linkage, rigid cube linkages and output platform of design-II. Using a screwdriver to assemble the output platform linkage is also shown in Figure 15f. Compared with design-I, design-II has less assembling errors. However, the monolithic structure, as shown in Figure 15c, of the practical design-II has to be made of a single material, and the whole structure should be replaced if only one of the compliant beams is broken.


Figure 15. Manufacture and assembling process of the practical design-II: (**a**) monolithically fabricated model, (**b**) demonstration of the vertex cubes, (**c**) monolithically fabricated model without the vertex cubes, (**d**) output platform linkage and rigid cube linkage assembly, (**e**) output platform assembly and (**f**) demonstration of using a screwdriver to assemble the output platform linkage.

7. System Design

The practical designs, design-I and design-II, have many potential applications such as micro-/nano-positioning platform and nano-manufacturing. This section presents a spatial high-precision translational manipulator, which is designed using the practical design-I or the practical design-II. The spatial high-precision translational manipulator is comprised of the practical design-I or the practical design-II, supporting stand, three actuators and displacement sensors, as shown in Figure 16a. The beam length, beam thickness and cube width of the spatial high-precision translational manipulator are 30, 1 and 20 mm, respectively. The peripheral dimension of the spatial high-precision translational manipulator is about 350 mm × 350 mm × 350 mm. This paper shows only the layout of the system design, while the detailed design for prototyping and experimental testing will be our further work. For the layout design, the following two key aspects should be emphasized: (a) displacement sensor assembling; and (b) actuator assembling.

In order to control the output platform at a specific position, the translational displacements of the output platform should be measured by a three-axis displacement sensor or three single-axis displacement sensors. If using three single-axis displacement sensors to measure the three translations of the output platform, each of the three single-axis displacement sensors should be capable of tolerating the other two displacements of the output platform. For convenience and decreasing the cost, we measure the displacements of the three rigid cube linkages instead of measuring the displacements of the output platform. The displacements of the three rigid cube linkages are almost the same as the displacements of the output platform along the three directions, respectively, because the lost motion rates of the proposed XYZ CPM are negligible. Furthermore, because each of the rigid cube linkages translates only along one specific direction, the displacement sensor measuring the displacement of the rigid cube linkage does not need to tolerate big transverse displacements along the other directions. Therefore, we can employ three accurate optical linear encoders to measure the displacements along the X-, Y- and Z-axes, respectively. Each optical linear encoder is comprised of a scale and a read head. The read head is used to read the encoded position from the scale. Figure 16b shows the assembly of the three optical linear encoders. The optical linear encoder, as shown in Figure 16b, is modeled based on a SIGNUM™ (Renishaw Public Limited Company, Gloucestershire, UK) RSLM/RELM high accuracy linear encoder system (the type number of the read head is A-9572-1514, and the type number of the scale is A-9660-0130), which can provide up to a 5-nm resolution.

Three cylindrical housed linear voice coil actuators (made by BEI Kimco Company located in Vista, CA, USA, and the type number of the actuator is LAH43-86-001Z) are selected to actuate the three translations of the high-precision spatial translational manipulator system, as shown in Figure 16a. The actuators can offer peak force 1512.4 N, continuous stall force 386.7 N and virtually unlimited resolution. The resolution is limited only by the associated displacement sensors. As analyzed in Section 4, the parasitic translations of the ASs are tiny. Therefore, the actuators do not suffer from off-axis displacements, even though the three actuators are rigidly connected to the three ASs, respectively. However, three flexure actuator linkages are still designed to connect the actuators with the ASs, which can be used to eliminate the assembly error effects of the actuators. Each of the flexure actuator linkages has a flexure beam, which is used to transmit the displacement from the actuator to the associated AS, as shown in Figure 16c. The flexure beam, as shown in Figure 16d, has one DOC along the beam and five DOF along and about other directions, so it can prevent the transmission of: (a) the assembly errors of the actuators to the ASs; and (b) the parasitic motions of the ASs to the actuators.
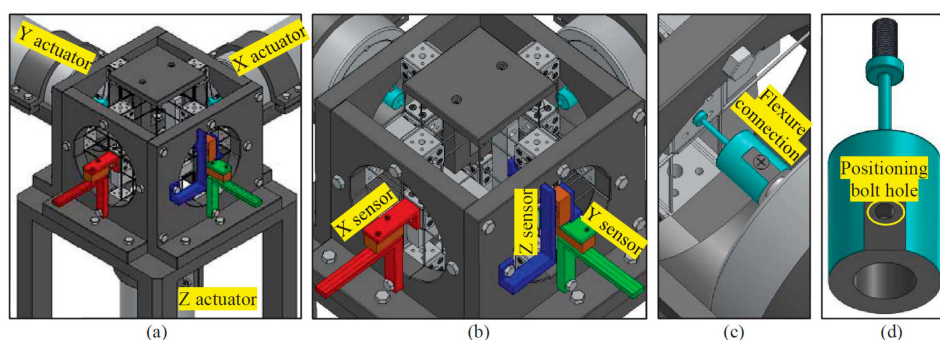
Figure 16. Demonstration of a spatial high-precision translational manipulator based on the practical design-I or design-II: (**a**) the spatial high-precision translational manipulator, (**b**) translational displacement measure sensor and (**c,d**) flexure actuator linkage.

8. Conclusions

This paper proposed a new, compact and symmetric XYZ CPM, using the CPI approach with a configuration modification. The designed XYZ CPM not only provides translations along the three orthogonal directions, but also has desired motion characteristics such as reduced cross-axis

coupling rates and minimized lost motion rates. It can be seen that the rigid stages of the XYZ CPM are over constrained by the wire beams, which is good for increasing the stiffness in the DOC directions. The stiffness in the DOF directions is also increased because of the overconstraints, which results in the increase of the actuation forces. However, the stiffness in the DOF directions is still small compared with the equivalent sheet-based XYZ CPMs. Moreover, the desired motion characteristics mentioned above were analyzed and validated by the FEA results, and the relations between the motion characteristics and the geometric parameters have been obtained. The primary translations of the XYZ CPM have also been analytically modeled, which can be used to quickly predict the actuation forces and actuation stiffness of an XYZ CPM. It can be seen that the good motion characteristics, especially the reduced cross-axis coupling rates and the minimized lost motion rates, can simplify the control system design.

Two practical designs of the new XYZ CPM were presented with consideration of the fabrication. The two practical designs can be used in many applications such as micro-/nano-manipulation. The layout design of a spatial high-precision translational system was also presented with consideration of the actuator and sensor integration. The further investigations including the physical prototyping, the experimental testing and the control system design, are our future work.

Author Contributions: Haiyang Li and Guangbo Hao conceived the ideas for the design and modelling of the XYZ Compliant Parallel Mechanism; Haiyang Li performed the FEA simulations and analyzed the data; Haiyang Li and Richard Kavanagh contributed to the practical designs of the XYZ Compliant Parallel Mechanism; Haiyang Li wrote the paper with the revision of Guangbo Hao and Richard Kavanagh.

Conflicts of Interest: The authors declare no conflict of interest.

References

1. Smith, S.T. *Flexures: Elements of Elastic Mechanisms*; Gordon and Breach Science Publishers: New York, NY, USA, 2000.
2. Howell, L.L. *Compliant Mechanisms*; John Wiley & Sons: New York, NY, USA, 2001.
3. Jones, R. Some uses of elasticity in instrument design. *J. Sci. Instrum.* **1962**, *39*, 193. [CrossRef]
4. Howell, L.L. *Handbook of Compliant Mechanisms*; John Wiley & Sons: New York, NY, USA, 2013.
5. Xu, Q. New flexure parallel-kinematic micropositioning system with large workspace. *IEEE Trans. Robot.* **2012**, *28*, 478–491. [CrossRef]
6. Hao, G. Towards the design of monolithic decoupled XYZ compliant parallel mechanisms for multi-function applications. *Mech. Sci.* **2013**, *4*, 291–302. [CrossRef]
7. Zhang, J.; Zhao, Y.; Dai, J. Compliance modeling and analysis of a 3-RPS parallel kinematic machine module. *Chin. J. Mech. Eng.* **2014**, *27*, 703–713. [CrossRef]
8. Xu, Q. Digital sliding mode prediction control of piezoelectric micro/nanopositioning system. *IEEE Trans. Control Syst. Technol.* **2015**, *23*, 297–304.
9. Awtar, S.; Ustick, J.; Sen, S. An XYZ parallel-kinematic flexure mechanism with geometrically decoupled degrees of freedom. *J. Mech. Robot.* **2012**, *5*, 015001. [CrossRef]
10. Hao, G.; Kong, X. Design and modeling of a large-range modular XYZ compliant parallel manipulator using identical spatial modules. *J. Mech. Robot.* **2012**, *4*, 021009. [CrossRef]
11. Hao, G.; Li, H. Design of 3-legged XYZ compliant parallel manipulators with minimised parasitic rotations. *Robotica* **2015**, *33*, 787–806. [CrossRef]
12. Li, Y.; Xu, Q. A totally decoupled piezo-driven XYZ flexure parallel micropositioning stage for micro/nanomanipulation. *IEEE Trans. Autom. Sci. Eng.* **2011**, *8*, 265–279. [CrossRef]
13. Schitter, G.; Thurner, P.J.; Hansma, P.K. Design and input-shaping control of a novel scanner for high-speed atomic force microscopy. *Mechatronics* **2008**, *18*, 282–288. [CrossRef]
14. Kozuka, H.; Arata, J.; Okuda, K.; Onaga, A.; Ohno, M.; Sano, A.; Fujimoto, H. A Bio-Inspired Compliant Parallel Mechanism for High-Precision Robots. In Proceedings of the IEEE International Conference on Robotics and Automation (ICRA), St. Paul, MN, USA, 14–18 May 2012; pp. 3122–3127.

15. Yu, J.; Bi, S.; Zong, G.; Liu, X.J. On the design of compliant-based micro-motion manipulators with a nanometer range resolution. In Proceedings of the IEEE/ASME International Conference on Advanced Intelligent Mechatronics, Kobe, Japan, 20–24 July 2003; Volume 1, pp. 149–154.

16. Chen, G.; Wilcox, D.L.; Howell, L.L. Fully compliant double tensural tristable micromechanisms (DTTM). *J. Micromech. Microeng.* **2009**, *19*, 025011. [CrossRef]

17. Hicks, T.R.; Atherton, P.D. *The Nanopositioning Book: Moving and Measuring to Better Than a Nanometre*; Queensgate Instruments Limited: Ann Arbor, MI, USA, 2000.

18. Li, H.; Hao, G. A constraint and position identification (CPI) approach for the synthesis of decoupled spatial translational compliant parallel manipulators. *Mech. Mach. Theory* **2015**, *90*, 59–83. [CrossRef]

19. Yue, C.; Zhang, Y.; Su, H.; Kong, X. Type synthesis of three-degree-of-freedom translational compliant parallel mechanisms. *J. Mech. Robot.* **2015**, *7*, 031012. [CrossRef]

20. Xu, Q.; Li, Y. A novel design of a 3-PRC translational compliant parallel micromanipulator for nanomanipulation. *Robotica* **2006**, *24*, 527–528. [CrossRef]

21. Hao, G.; Li, H. Conceptual designs of multi-degree of freedom compliant parallel manipulators composed of wire-beam based compliant mechanisms. *Proc. Inst. Mech. Eng. C J. Mech. Eng. Sci.* **2015**, *229*, 538–555. [CrossRef]

22. Blanding, D.L. *Exact Constraint: Machine Design Using Kinematic Principles*; ASME: New York, NY, USA, 1999.

23. Awtar, S.; Slocum, A.H. Constraint-based design of parallel kinematic XY flexure mechanisms. *J. Mech. Des.* **2006**, *129*, 816–830. [CrossRef]

24. Su, H.; Dorozhkin, D.V.; Vance, J.M. A screw theory approach for the conceptual design of flexible joints for compliant mechanisms. *J. Mech. Robot.* **2009**, *1*, 041009. [CrossRef]

25. Hopkins, J.B.; Culpepper, M.L. Synthesis of multi-degree of freedom, parallel flexure system concepts via freedom and constraint topology (FACT)-Part I: principles. *Precis. Eng.* **2010**, *34*, 259–270. [CrossRef]

26. Hopkins, J.B.; Culpepper, M.L. Synthesis of multi-degree of freedom, parallel flexure system concepts via freedom and constraint topology (FACT)-Part II: Practice. *Precis. Eng.* **2010**, *34*, 271–278. [CrossRef]

27. Hao, G.; Yu, J. A completely kinematostatically decoupled XY compliant parallel manipulator through a new topology structure. In Proceedings of the IFToMM Workshop on Fundamental Issues and Future Research Directions for Parallel Mechanisms and Manipulators, Tianjin, China, 7–8 July 2014.

28. Yu, J.; Xie, Y.; Li, Z.; Hao, G. Design and experimental testing of an improved large-range decoupled XY compliant parallel micromanipulator. *J. Mech. Robot.* **2015**, *7*, 044503. [CrossRef]

29. Awtar, S. *Synthesis and Analysis of Parallel Kinematic XY Flexure Mechanisms*; Massachusetts Institute of Technology: Cambridge, MA, USA, 2004.

30. Li, H.; Hao, G. Constraint-force-based (CFB) modelling of compliant mechanisms. In Proceedings of the ASME 2015 International Design Engineering Technical Conferences & Computers and Information in Engineering Conference, Boston, MA, USA, 2–5 August 2015.

31. Hao, G.; Kong, X.; Reuben, R.L. A nonlinear analysis of spatial compliant parallel modules: Multi-beam modules. *Mech. Mach. Theory* **2011**, *46*, 680–706. [CrossRef]